Dynamics of Atmospheres and Oceans 50 (2010) 16–34

Contents lists available at ScienceDirect

Dynamics of Atmospheres and Oceans

journal homepage: www.elsevier.com/locate/dynatmoce

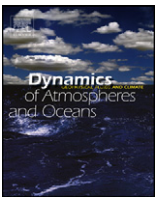

Experimental observation of strong mixing due to internal wave focusing over sloping terrain

Arno Swart[a,*], Astrid Manders[b,1], Uwe Harlander[c,2], Leo R.M. Maas[d,e,3]

[a] *RIVM - Centre for Infectious Disease Control, Laboratory for Zoonoses and Environmental Microbiology-LZO, P.O. Box 1 (internal mailbox 63), 3720 BA Bilthoven, The Netherlands*
[b] *TNO Built Environment and Geosciences, Unit Environment, Health and Safety, P.O. Box 80015, 3508 TA Utrecht, The Netherlands*
[c] *Department of Aerodynamics and Fluid Mechanics, Brandenburg University of Technology (BTU) Cottbus, Siemens-Halske-Ring 14, D-03046 Cottbus, Germany*
[d] *Netherlands Institute for Sea Research, P.O. Box 59, 1790 AB Texel, The Netherlands*
[e] *Institute for Marine and Atmospheric Research Utrecht, Buys Ballot Laboratorium, Princetonplein 5, 3584 CC, Utrecht, The Netherlands*

ARTICLE INFO

Article history:
Received 18 September 2008
Received in revised form 13 August 2009
Accepted 19 August 2009
Available online 3 September 2009

Keywords:
Mixing
Internal waves
Wave attractors
Rotating stratified fluids
Boundary layers
Boundary layer eruptions

ABSTRACT

This paper reports on experimental observation of internal waves that are focused due to a sloping topography. A remarkable mixing of the density field was observed. This result is of importance for the deep ocean, where internal waves are believed to play a role in mixing. The experiments were performed on the rotating platform at the Coriolis Laboratory, Grenoble. The rotation, its modulation and density stratification were set to be in the internal wave regime. After applying various data processing techniques we observe internal wave rays, which converge to a limiting state: the wave attractor. At longer time scales we observe a remarkably efficient mixing of the density field, possibly responsible for driving observed sheared mean flows and topographic Rossby waves. We offer the hypothesis that focusing of internal waves to the wave attractor leads to the mixing.

* Corresponding author. Tel.: +31 030 274 2090.
E-mail addresses: arno.swart@rivm.nl (A. Swart), astrid.manders@rivm.nl (A. Manders), haruwe@tu-cottbus.de (U. Harlander), maas@nioz.nl, l.r.m.maas@uu.nl (L.R.M. Maas).
[1] Tel.: +31 88 8662260.
[2] Tel.: +49 355 695121; fax: +49 355 694891.
[3] Tel.: +31 222 369419/30 253 2715; fax: +31 222 319674/30 254 3163.

0377-0265/$ – see front matter © 2009 Elsevier B.V. All rights reserved.
doi:10.1016/j.dynatmoce.2009.08.003

1. Introduction

The mixing of rotating stratified fluids is of great interest in the fields of geophysical fluid dynamics and is of relevance for understanding the physics of the oceans. Particularly interesting is the fact that internal wave breaking may contribute to mixing in the deep ocean (e.g. Ledwell et al., 2000; Staquet and Sommeria, 2002).

We have set up a laboratory experiment, aiming to collect evidence for the hypothesis that internal wave reflections can lead to strong localized mixing.

In our experimental setup a stratified fluid is contained in a rotating annulus, with sloping inner wall. This setup mimics the topography of an ocean abyssal plane and continental slope. In order to excite waves, we applied a weak modulation of the rotation rate, on top of a solid body rotation. This modulation rate was chosen at a frequency where we theoretically expect a *wave attractor*. Section 2 gives the theoretical background on wave attractors in rotating stratified fluids. Section 3 describes our experimental setup. Evidence for the manifestation of the attractor in our experiment is presented in Section 4.

Despite the fact that we do not disturb the fluid in any mechanical way, other than by weak modulation, we observe very strong mixing, much stronger than seen in similar experiments that lack the periodic modulation. We offer the hypothesis that the focusing action of internal waves, reflecting at the sloping boundary is responsible for this mixing. Firstly, we present density profiles in Section 4.1 that clearly show that at the end of the experiment the density gradient has been heavily modified. We argue that the modulation is responsible for a localized wave beam. In the traditional view, this beam is formed at the critical convex slope, where the wave characteristic equals the bottom slope, but which is not present in our experiment. We add here an additional view and argue that the beam might also result from an eruption of the boundary layer at a concave critical slope, which directly forces internal waves. In the appendix we discuss a theoretical model which predicts these eruptions and we present direct measurements of the boundary layer eruption in Section 4.2. Furthermore, we experimentally establish the existence of a wave attractor (Section 4.3) which could theoretically further enhance the mixing. The wave attractor was observed in a vertical plane.

While Section 4 focuses on direct measurements of mixing and internal waves, Section 5 presents measurements of waves and flows that are *caused* by the mixing. A mean flow may be indicative of internal wave breaking. In Section 5.1, we discuss observations of such a mean flow that occurs over the sloping inner wall. Additionally, in Section 5.2, we establish the occurrence of Rossby waves, which are also representative of local mixing.

Summarizing, we describe an experiment aimed at the validation of the following scenario

1. Boundary layer eruptions may generate gravito-inertial waves at critical angles of the sloping boundary of which only the concave one is present in our setup
2. These waves locally mix the density profile upon reflection at the boundary
3. Wave attractors may form, leading to increased mixing efficiency
4. As a result of the mixing, a measurable mean flow ensues and baroclinic/barotropic instability develops. In our experiment this leads to Rossby waves.

We believe that analysis of the collected data supports our claims. Mixing, wave attractors, mean flow generation and Rossby waves have been observed and the observations fit well into our theoretical framework.

2. Wave attractors and ray dynamics

Continuously stratified or rotating fluids support obliquely propagating internal waves. In a channel-like geometry, characterized by cross-channel topographic variations, internal wave beams are focused upon reflection at a slope. Ultimately these reflections may lead to so-called wave attractors (Maas and Lam, 1995; Drijfhout and Maas, 2008), see a review in Maas (2005). An oblique, free internal wavy boundary layer develops around the attractor location. Earlier exploratory laboratory studies have identified the existence and structure of such wave attractors both in uniformly stratified

fluids (Maas et al., 1997; Lam and Maas, 2008; Hazewinkel et al., 2008), as well as in non-axisymmetric rotating homogeneous fluids (Maas, 2001; Manders and Maas, 2003, 2004). In the former case these were excited by vertical and horizontal oscillations of the tank, while in homogeneous rotating fluids these were excited by modulation of the container's rotation speed. Here we explore their occurrence in an annulus with sloping inner boundary (see Fig. 1), in a fluid that is both uniformly stratified as well as rotating. We again employ modulation of the rotation speed as an axisymmetric forcing mechanism, producing monochromatic wave motion with frequency $\omega > 0$. Since the domain D is rotationally symmetric around the z-axis (see fig. 1) we use cylindrical (r, θ, z)-coordinates and search for axisymmetric solutions. In the interior of the fluid we assume the viscosity and diffusivity to be small and negligible (Batchelor, 1967). In this case the equation and boundary condition governing the internal wave spatial structure are

$$\begin{aligned} &\Psi_{rr} - \lambda^2 \Psi_{zz} = (r^{-1}\Psi)_r \equiv F(\Psi, r), \quad \text{in } D, \\ &\Psi = 0 \quad \text{at } \partial D, \end{aligned} \tag{1}$$

where Ψ is the stream function. This defines velocities u, w in radial and vertical directions by $(\Psi_z, -\Psi_r) = (ru, rw)$. For large values of r, neglecting the term$(r^{-1}\Psi)_r$, Eq. (1) becomes the Poincaré equation describing internal waves in rotating stratified fluids (Maas and Lam, 1995; Swart, 2007). The parameter λ is given by

$$\lambda^2 = \frac{\omega^2 - f^2}{N^2 - \omega^2}, \tag{2}$$

where f is the Coriolis parameter (measuring the importance of rotation) and N is the stability frequency (measuring the importance of stratification), here taken constant as in our experimental setup. Our experiment is such that $f^2 < \omega^2 < N^2$, so that Eq. (1) is of hyperbolic type.

Due to viscous effects, at the boundary ∂D of the fluid domain D, the fluid must co-rotate with the reference frame, which implies $\mathbf{u} = 0$. However, we take into account the existence of a boundary layer where the fluid adjusts from the frictional influence of the boundary. Because of the presence of these boundary layers, we have to good approximation a frictionless boundary between the interior and the boundary layer region. This justifies posing boundary conditions $\mathbf{u} \cdot \mathbf{n} = 0$ for the interior flow, with $\mathbf{n}$ the unit outward normal to the boundary.

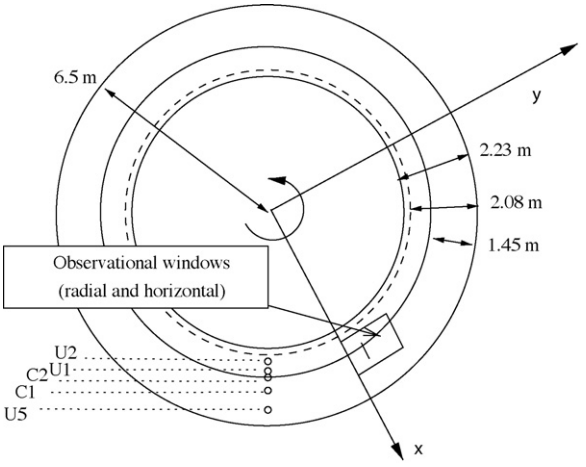

Fig. 1. This figure shows a schematic picture of the Coriolis turntable. The outer rim is located at 6.5 m. The inner circle represents the intersection of the water surface with the slope, while the middle solid circle is the start of the slope. The dashed line is the reflection of the attractor (see Fig. 2) at the slope. Also indicated are the radial positions of the probes C1, C2 and U1, U2, U5, and the observational window. The vertical z-axis in the middle is parallel to the rotation axis and points out of the paper.

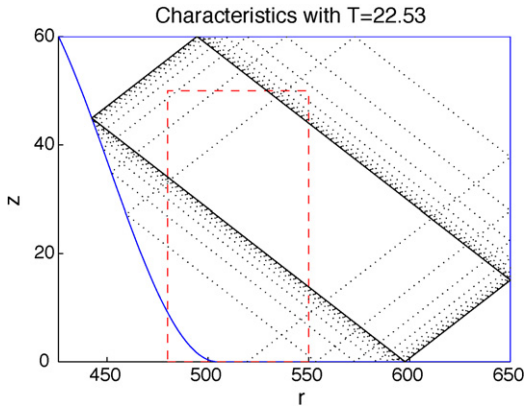

Fig. 2. This panel shows the skeleton of characteristics (4) in a radial (r, z) cross-sectional plane for frequency $\omega = 0.279$ rad s^{-1}. Distances are in centimeters and are measured outwards from the rotation axis and from the bottom of the tank respectively. The dotted line shows the approach of the characteristics to the (1,1)-attractor, given by the solid line. The dashed rectangle indicates the field of observation employed in the experiment.

The dispersion relation can be obtained by assuming wave motion $\Psi(r, z) = \Re[\hat{\Psi} e^{i(kr+mz)}]$. For simplicity we also set the right-hand side of (1) to zero, which is justified for $r \gg 1$. This approximation is not crucial (see e.g. Harlander and Maas, 2007; Lyashenko and Smiley, 1995), but it greatly simplifies the following discussion. In polar coordinates the wave vector is $\mathbf{k} = (k, m) = K(\sin(\alpha), \cos(\alpha))$, where the angle α is measured with respect to the vertical. This yields

$$\omega^2 = f^2 \cos^2(\alpha) + N^2 \sin^2(\alpha), \quad \text{and} \quad \lambda = \pm \tan(\alpha). \tag{3}$$

Phase and energy propagation are mutually perpendicular, while sharing the same horizontal propagation direction. As shown in Maas and Lam (1995) we can construct a 'skeleton' of the solution of (1) by considering the characteristics , namely

$$\begin{aligned} \xi(r, z) &= r - \lambda^{-1} z, \\ \eta(r, z) &= r + \lambda^{-1} z. \end{aligned} \tag{4}$$

The levelsets of these characteristics define two families of straight lines. The angle that the characteristic lines make with respect to the vertical is equal to the angle that the group velocity makes with the vertical, and is at right angles with the phase velocity vector. We conclude that energy propagation is in the direction of the characteristic lines. The precise behaviour along a characteristic is determined by the function F in (1), we are however only concerned with the singularity at the wave attractor. For numerical results in the case of non-zero F, see Harlander and Maas (2007).

The location of the wave attractor can be found by a ray-tracing procedure (see also Maas and Lam, 1995). Starting at a boundary point one traces characteristics from boundary point to boundary point. The fixed angle of the characteristics with the vertical, and the shape of the container, in general causes them to converge to a limit cycle termed the *wave attractor*. Fig. 2 shows the web of characteristics for the frequency used in the experiment. This frequency was carefully selected from numerical ray tracing experiments in order to obtain a simple wave attractor, having only four intersections with the boundary.

The inviscid solutions predict an infinite energy density along the attractor, since spatial scales will become arbitrarily small and the kinetic energy density becomes singular at the attractor (Swart et al., 2007). Viscosity (ν), diffusivity (κ) and non-linearity (not present in our model) will regularize the solution, creating high amplitude shear layers along the attractor.

As a final remark we point out that in the long run mixing modifies the density stratification, leading to curving of the characteristics, and, for strong perturbations, to internal wave scattering within the interior of the fluid. This may ultimately destroy the attractor. However, if the mixing is modest, then

the attractor may survive for some time. When choosing the frequency for use in our experiment, we made sure to pick one close to the center of the frequency interval where the (1,1)-attractor lives (the attractor with one reflection at both sides and one reflection at the top/bottom). This guarantees that the attractor is stable with respect to density variations. Small variations in stratification may alter the attractor slightly, but will not destroy it as long as the density perturbation is modest (see also the first chapter of Swart (2007)). In Manders and Maas (2004) the effect of frequency and domain perturbation on solutions in a specific geometry are studied.

3. Experimental setup

The experiment was carried out at the Coriolis turntable in Grenoble. This turntable consists of a rotating basin, having a diameter of thirteen meters. On the inner rim of the platform an axisymmetric sloping topography is mounted, the outer rim is vertical. The resulting axisymmetric annulus was filled with a uniformly stratified fluid. See Fig. 1 for a schematic representation of the turntable and its dimensions.

In the experiment we utilize two restoring mechanisms that give rise to internal wave motion. These are due to the Coriolis and buoyancy forces, owing to a stable stratification in angular momentum and density respectively. In a solid body rotation with period $T_0 = 50\,\mathrm{s}$ and frequency $\Omega_0 = 2\pi/T_0 = 0.126\,\mathrm{rad\,s^{-1}}$, the Coriolis parameter $f = 2\Omega_0 = 0.251\,\mathrm{rad\,s^{-1}}$. Initially, the fluid was uniformly stratified. The density stratification was set to $N = 2f = 0.502\,\mathrm{rad\,s^{-1}}$. Each experiment starts by modulating the angular velocity with a period of $T = 22.53\,\mathrm{s}$ giving a frequency of the generated internal waves of $\omega = 2\pi/T = 0.279\,\mathrm{rad\,s^{-1}}$. The amplitude of the modulation was chosen to be small compared to the amplitude of the solid rotation. The resulting angular frequency is

$$\Omega(t) = \Omega_0[1 + \epsilon\,\sin(\omega t)], \quad \text{for } 0 < \epsilon \ll 1.$$

We have set the amplitude of the azimuthal velocity modulation, attained at the outer rim ($R = 6.5\,\mathrm{m}$), to $v_{rim} = 6\,\mathrm{cm/s}$. Relative to the solid body rotation, this yields an amplitude of modulation $\epsilon = v_{rim}/(\Omega_0 R) \approx 0.07$. A convenient side effect of having a density stratification is that it leads to homogeneously distributed particles, that were added to the fluid for visualisation purposes. The particles have slightly differing density, which makes them float on different isopycnal layers where gravity and buoyancy are in equilibrium. The stratification is stable, therefore particles will execute vertical motions around their rest level due to waves.

The velocities of the particles are measured using the *particle image velocimetry* (PIV) technique (Fincham and Spedding, 1997). To this end particles are illuminated using a laser sheet. The laser is mounted on the turntable in such a way as to produce either radial or horizontal sheets. The particles in the laser sheet are then photographed using a camera that is also mounted on the turntable. The camera sampling rate has been set to obtain eight velocity fields per wave period. Each single velocity field is created from four pictures, which are rapidly taken in a very small time interval (in the order of milliseconds), a *burst*. A time series of bursts is further processed by PIV software to create the velocity vector fields. These velocities are our basic fields, which need further processing.

In addition to the PIV velocity measurements, also density profiles were obtained by moving conductivity probes vertically (see Fig. 1).

4. Results

In the experiments very strong mixing was observed. This might seem remarkable at first sight, since we do not disturb the fluid in any direct way. The axisymmetric turntable is merely rotated and weakly modulated. No traditional source of mixing seems to be present. Yet, as described in Section 4.2 we have a mechanism for wave generation plus the possibility of focusing reflection of internal waves at the sloping boundary, which leads to intensification and mixing. We will make plausible in the following sections that this scenario indeed occurred.

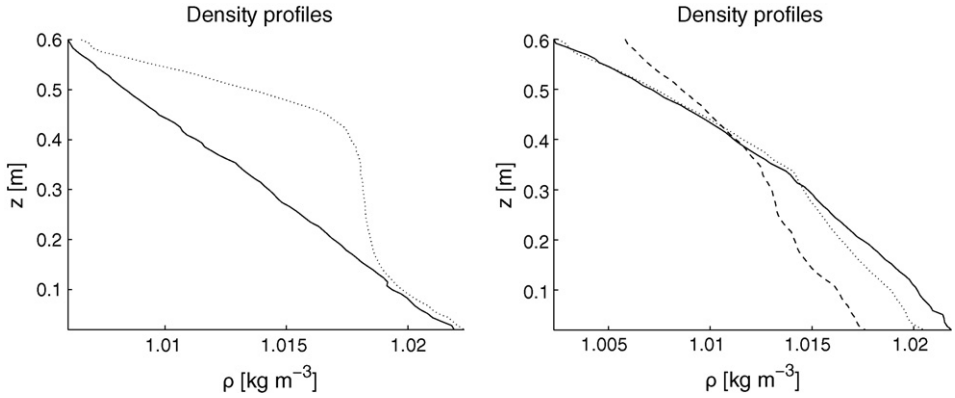

Fig. 3. Density profiles showing the mixing that has taken place during two separate experiments. Solid lines indicate the initial profile, dotted lines the final profile after 63 h (left panel) and 1 h (right panel). The dashed profile in the right panel shows the distribution 3 h after modulation was stopped. Both profiles were taken from probe C2 (see Fig. 1) at $T = 22.53$ s, corresponding to the (1,1)-attractor.

4.1. Mixing

Firstly we argue that we indeed observed mixing from the probe data (Fig. 3), obtained from probe C2 (see Fig. 1 for the location of probe C2). The leftmost panel represents a rather extreme experiment where modulation was on for 6 h, after which the turntable rotated steadily and another profile was measured 63 h later (the dotted line). The initially linear stratification (solid line) was heavily modified. This is quite extraordinary as experience with previous experiments learned that the stratification could be maintained while uniformly rotating for periods up to 1 month (Sommeria, 2007, personal communication). The rightmost panel was an experiment where modulation was turned on for a shorter time. The profiles before (solid) and after (dotted) 1 h of modulation already show that mixing was in effect. But, even after modulation was stopped there was additional mixing as can be seen from the dashed profile which was taken 3 h after modulation was stopped. Of course internal waves continue to travel and reflect at sloping surfaces where they focus, amplify, and break (which explains the ongoing mixing) until the waves are ultimately damped by viscous or nonlinear processes.

Note that in the leftmost panel of Fig. 3 mass appears not to be conserved. Density still increases with depth, but more mass is present at lower depths. The profiles were taken at one fixed position. It is unlikely that density varies in the azimuthal direction, which implies that density is redistributed in the radial and vertical directions. Since denser fluid is now present above the foot of the slope, lighter fluid must be present at the outer rim. We speculate as to its causes in Section 5. Of course, the apparent violation of mass conservation might also be due to a drift in the measurements made by the probes, yielding flawed observations. This does however not diminish the conclusion that strong mixing has occurred.

4.2. Forcing of internal waves

In this and the following subsection, we use PIV data obtained in a radial plane, the dashed rectangle indicated in Fig. 2. The observations provide a time series of radial and vertical velocities. We segmented the data in time intervals of 50 pictures, corresponding to 147 s or approximately 6.3 wave periods each. The internal wave shearing motion implies that in the plane of observation the magnitude of the vorticity (curl of velocity) field will be a good indicator of the presence of internal wave beams. We therefore compute the curl of the velocity field, and calculate its phase and amplitude using an harmonic analysis for each time interval. Additionally, we use an Empirical Orthogonal Function (EOF) decomposition (Storch and Zwiers, 1999) in order to filter out unwanted noise from the data.

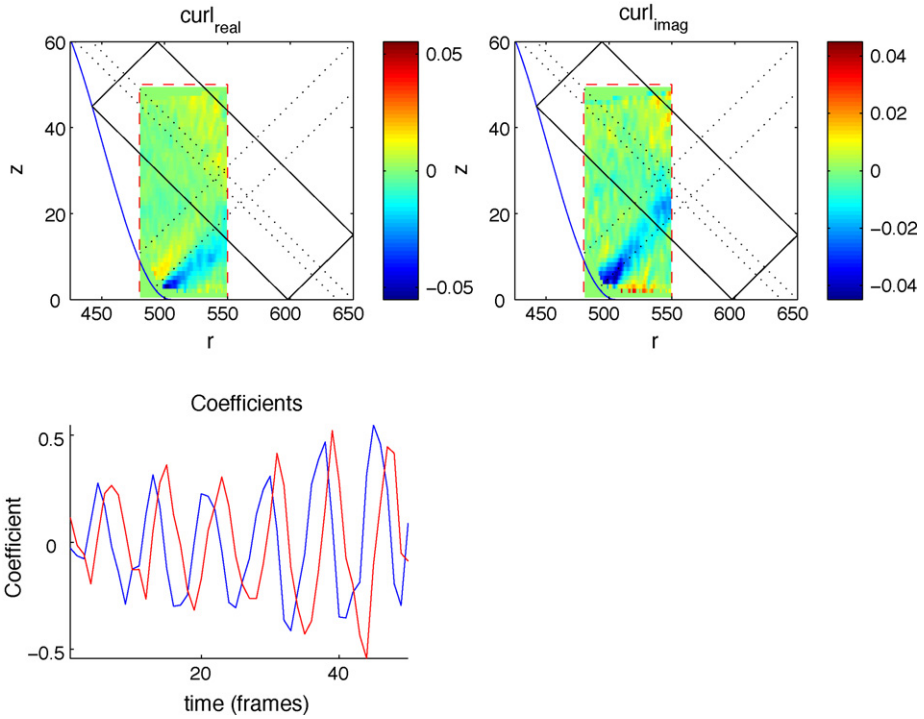

Fig. 4. The lower panel shows the amplitudes of a Hilbert EOF and corresponding real (upper left panel) and imaginary (upper right panel) vorticity fields [s^{-1}] in a radial r, z-plane (again measured in cm from the rotation axis outwards and from the bottom upwards). The signal is well represented by a superposition of both images with amplitudes that evolve in time as in the lower panel. Red/blue lines indicate the amplitude of the real and imaginary parts. We see that the beam grows in amplitude while coming into existence in an oscillating manner, with a frequency equal to the modulation frequency, remembering that we sample 8 frames per wave period.

The EOFs are orthogonal spatial patterns that can be seen as empirically derived basis functions. Frequently, the low-order EOFs are interpreted as the natural modes of variability of an observed system although some caution is called for since EOFs do not represent physical fields a priori. We expect that this representation emphasizes the main features of the attractor. Aside from standard EOFs, which ignore the time evolution of the analyzed field, we will also use Hilbert EOFs. Hilbert EOF's (sometimes also called complex EOFs) account for patterns that evolve in time, presented by real and imaginary parts of the EOF between which the pattern oscillates.

In the time interval 0–147 s, at the start of the modulation, we observe the development of a beam, emanating from the bottom-left corner (Fig. 4). We estimate the beam to have a width of approximately 10 cm. Maximum vorticity amplitudes increase from 0 to 0.06 s^{-1} in six wave periods. Phase propagation is downwards and to the right, as would be observed by viewing a movie of the curl fields. This implies energy propagating upward and to the right, away from the corner. The phenomenon of beams emanating from corners was noticed before by Beardsley (1970), in an experiment similar to ours in a homogeneous fluid. Since it is likely that similar beams could emanate from other corners of the basin we overlay the corresponding characteristics in the figures (the dotted lines in Fig. 4 and following figures). However, even with this visual aid such beams are not visible in the pictures.

Several hypotheses can be put forth concerning the origin of the wave beam.

Traditionally, an inviscid theory is employed for explaining internal wave generation (and mixing) at continental slopes (Baines, 1982). In the oceans, internal tides are believed to be generated over continental slopes due to tidal motion in the cross-slope direction, that lifts and depresses isopycnals.

An alternative viewpoint is offered by 'internal tides', generated by oscillating cylinders in a stratified fluid, that matches well with beams predicted by a viscous theory (Gostiaux and Dauxois, 2007). In our experiments, however, the 'tidal' flow corresponds to a purely axisymmetric flow, apparently lacking such a cross-isobath component. Close to the bottom, however, since the fluid has a nonzero velocity with respect to the co-rotating frame of reference, the azimuthal flow is retarded by frictional forces. This is then deflected in the boundary layer into the radial direction by Coriolis forces, leading to cross-slope oriented oscillatory currents (Thorade, 1928; Prandle, 1982; Maas et al., 1987), a barotropic sloshing. This boundary layer is an oscillatory version of the *Ekman layer*. This mechanism may lead to mixing in a direct way, due to static instability, when light water is transported below heavier water (Ramsden, 1995).

Using this viscous process for creating a shoreward flow in the first place, the traditional inviscid mechanism for internal wave generation may come into play. However, in the inviscid forcing mechanism the strongest generation site is usually observed at points of convex curvature, such as the shelf edge (Legg and Adcroft, 2003). In our experiments the shelf edge lies, however, outside our fluid domain and we observe wave generation over a concave slope. This does not imply that conversion of barotropic sloshing into baroclinic waves is entirely absent, but the observations suggest these waves must be of small amplitude and large scale, since in our experiment they appear to be overshadowed by the internal wave beam directly stemming from the lower left corner.

Here we present therefore a novel approach, where the wave beam is induced by viscous effects in the boundary layer. Our exposition (Appendix A) retains both rotation and background stratification. Also both viscosity and thermal diffusivity are included. We do this in an axisymmetric setting. In order to obtain tractable equations, we take into account the large radius of the geometry and assume velocities to vary in a direction perpendicular to the boundary only. We derive Eq. (15) for the boundary layer depth for oscillating flow. This equation has the important property that this boundary layer depth becomes singular at so-called critical angles, where bottom slope β equals characteristic slope α; i.e. $\beta = k\pi \pm \alpha$, with $k \in \mathbb{N}$. For the specific case treated in our laboratory experiment only one of these angles is, strictly speaking, present in the geometry: at the sloping bottom in the lower left corner where the slope varies continuously. However, it might be argued that critical angles also are present in the other, right and acute angled corners, where the slope varies discontinuously.

We put forth this localized viscous boundary layer eruption as a forcing mechanism for internal waves. The other mechanisms leading to internal wave generation and mixing may also contribute to the overall mixing. However, they do not seem to explain the magnitude of the observed mixing, nor to generate wave beams at the observed locations.

Note that such boundary layer eruptions were reported before in Greenspan (1968); Kerswell (1995) and Hollerbach and Kerswell (1995), where the authors study internal shear layers spawned at critical angles in co-axial and spherical configurations. In these papers, the boundary layer eruptions generating internal shear layers were established both analytically and numerically. An experiment in Beardsley (1970) documents such an event, as wave rays are seen to emanate from the corners of a rotating truncated cone.

4.3. Formation of the attractor

This section presents an analysis of the formation of the internal wave attractor. We present vertical cross-sections of the fluid domain, and discuss the formation of the attractor using amplitude and phase pictures. The presence of the attractor is established from the observation of high amplitudes at the attractor location, consistent phase behaviour, and the emergence of higher harmonics.

148–249 s, Fig. 5 (a)

After approximately 4 min a second beam becomes visible. The location of the beam shows that it is likely that we see the attractor and not a direct beam from the corner. The phase is harder to interpret. Just above the lower left attractor leg the direction of phase propagation is downwards and to the left, while below the attractor leg the phase propagation is upwards and to the right. This could indicate a standing wave character in this initial phase of attractor formation, consistent with the findings of

Maas et al. (1997). Second harmonics (not shown) were found to have amplitudes of a factor 10 less, and are insignificant at this point.

250–441 s, Fig. 5(b)

The harmonic analysis shows largely the same picture as before, but the amplitude at the attractor location has grown. Again, the phase seems to indicate a standing wave. Since the next interval (442–558 s) shows largely the same features as the current interval, we skip this interval.

589–735 s, Fig. 5(c)

The main feature in the first harmonics (top panels) is a second beam, visible just above the bottom segment of the attractor. This could be due to a boundary layer eruption from the bottom-right corner of the domain.

Second harmonics (bottom panels) have now developed, mainly along the attractor location, with amplitude one fifth of the first harmonic. Although we have neglected the usual nonlinear term $\mathbf{u} \cdot \nabla \mathbf{u}$ in our model equations, in reality this term can become significant when $\nabla \mathbf{u}$ is large. This is particularly

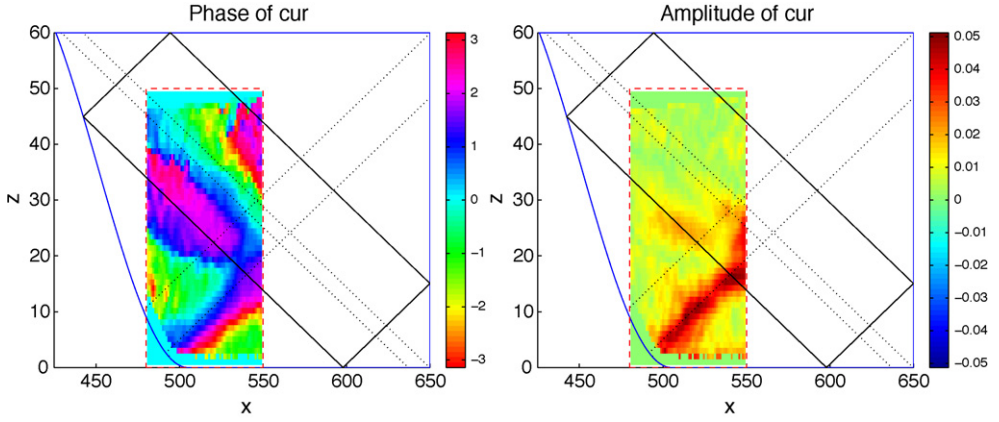

(a) Wave periods 7 to 12. The direct beam has a high amplitude and the phase corresponds to the velocities observed in a movie of the direct velocity fields.

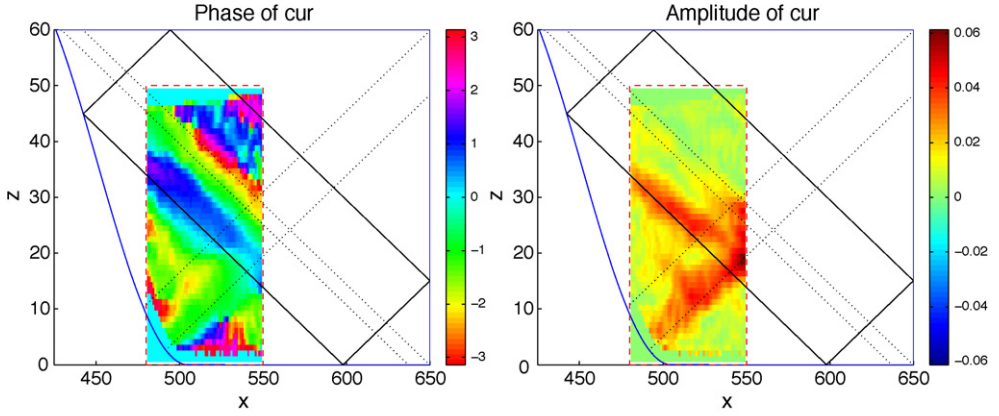

(b) Wave periods 13 to 18. Comparison to Fig. 5(a) reveals that the amplitude at the predicted attractor location has grown.

Fig. 5. These panels show the phase field (left) and amplitude field (right) of the curl of the velocities, obtained by harmonic analysis. (a) Wave periods 7–12. The direct beam has a high amplitude and the phase corresponds to the velocities observed in a movie of the direct velocity fields. (b) Wave periods 13–18. Comparison to (a) reveals that the amplitude at the predicted attractor location has grown. (c) Wave periods 25–30. The bottom row represents the second harmonic.

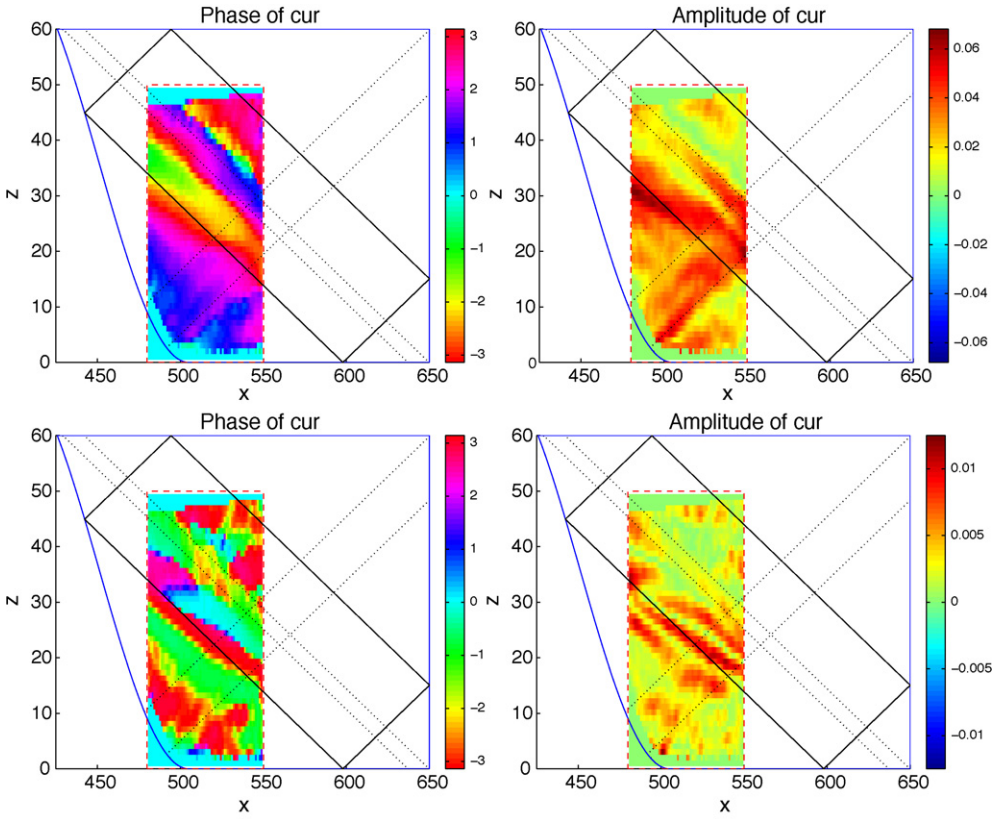

Fig. 5. (*Continued*).

the case when beams overlap and may lead to the generation of higher harmonic waves of frequency $n\omega$, $n \in \mathbb{N}$, that can propagate away as free waves, and under a steeper angle, as long as $\lambda^2 > 0$ in, Eq. (2), upon replacing ω by $n\omega$. Nonlinear effects at the attractor location may, however, also induce forced harmonics that do not follow the dispersion relation of free waves, and do not propagate away (Lam and Maas, 2008). This appears to be the case in the present experiment, as the second harmonic's spatial structure coincides with that of the first harmonic. See (e.g. Greenspan, 1968, p. 215) for a general discussion of generation of higher harmonics.

736–882 s, Fig. 6(a)

In this picture we observe a strong beam just above the slope, it might be the reflection of the beam from the bottom left corner, after two reflections. At the sloping wall it is focused, which would explain its increase in amplitude. The phase pictures are very clear, yet the amplitude pictures become difficult to interpret. The downward propagating phase at the top right corner of the observational window is consistent with the 'upper leg' of the attractor.

The amplitude of the second harmonic has grown, and is now comparable to that of the first harmonic. In the phase picture we see perfect anti-phase, indicating it grows as a standing wave. For the phenomenon of anti-phase there is numerical evidence (e.g. Swart et al., 2007; Swart, 2007) and it has also been observed in the laboratory (e.g. Maas et al., 1997).

>3600 s, Fig. 6(b)

From this point on the situation is too messy to draw any conclusions. In the long term the phase and amplitude lines do no longer follow the characteristic directions, but become flatter. It is likely that mixing has modified the stratification to such an extent as to modify the direction of wave rays

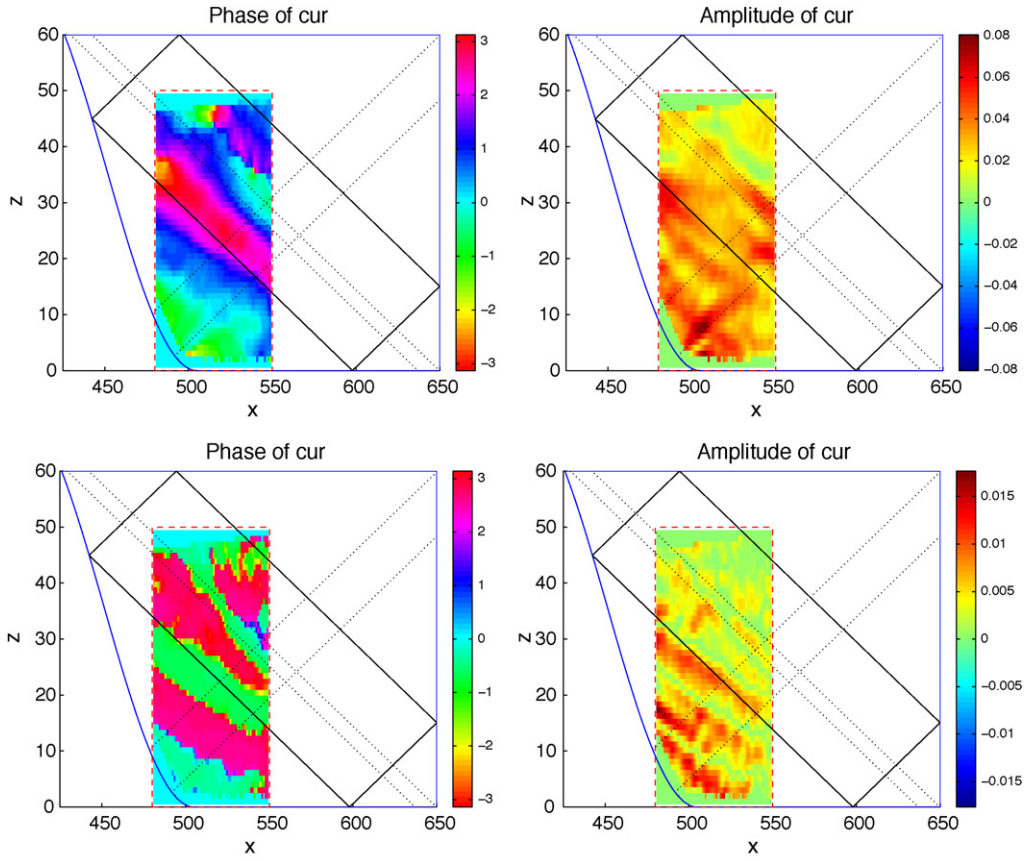

(a) Wave periods 31 to 36. There is now a clear beam above the slope, whose amplitude is comparable to that of the attractor. The bottom row represents the second harmonic.

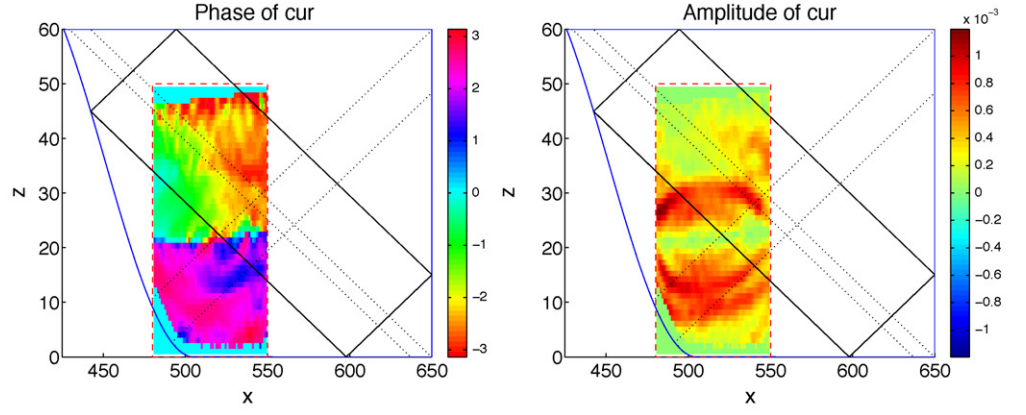

(b) After approximately one hour of modulation and half an hour of solid body rotation the attractor was destroyed.

Fig. 6. This figure continues Fig. 5. (a) Wave periods 31–36. There is now a clear beam above the slope, whose amplitude is comparable to that of the attractor. The bottom row represents the second harmonic. (b) After approximately 1 h of modulation and half an hour of solid body rotation the attractor was destroyed.

and inhibit the further formation of the attractor. The beam above the slope however, was found to be present also for longer time scales. After 1 h of modulation, and half an hour of solid body rotation the attractor was completely destroyed as can be seen in Fig. 6(b).

5. Secondary phenomena

We now proceed with the discussion of two consequences of the mixing process, the generation of a localized unstable mean flow and subsequent generation of Rossby waves.

5.1. Azimuthal mean flow

Consider the azimuthal mean of the time mean azimuthal velocity field, top panel of Fig. 7, observed from above, as shown in Fig. 1. The azimuthal mean velocity shows a prominent band of negative (retrograde) velocity somewhat left of the center of the annulus ($525 < r < 600$ cm), and a narrower band of positive (prograde) velocity above the inner, sloping boundary and foot of the slope ($500 < r < 525$ cm). Note that the maximum of the mean flow is about 12% of the amplitude of the time harmonic component of internal waves at the forcing frequency. A (barotropic) multiple jet flow of the type shown in the top panel of Fig. 7 is typically unstable. Thus the occurrence of such a mean

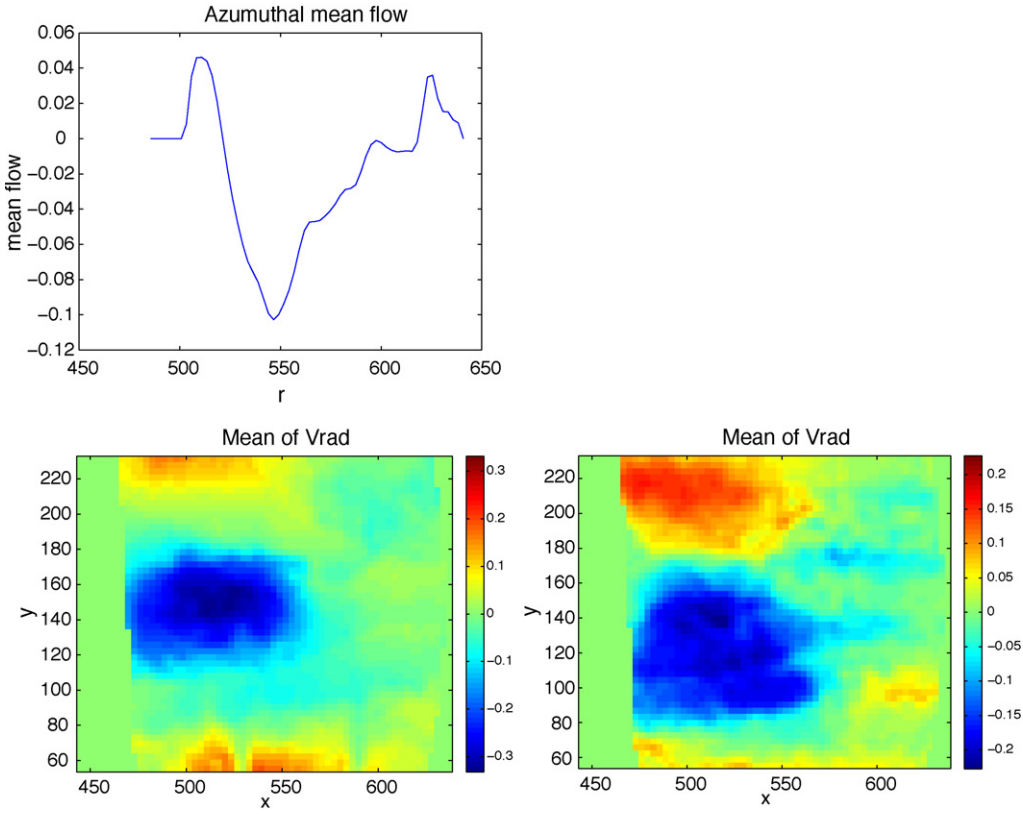

Fig. 7. Top panel: time mean of the spatially averaged azimuthal flow field in m/s as a function of radial distance r in cm. The shelf is on the left side of the figure and the foot of the slope is at $r = 505$ cm. Bottom panels: spatial velocity fields in a horizontal plane at 8 cm below the surface. Mean radial velocity field in m/s (color). Cartesian x, y coordinates (in cm) as in Fig. 1 (x corresponds in good approximation with radial coordinate r). The two figures are three modulation periods apart. The wave propagates in retrograde direction, towards smaller values of y.

flow could explain the existence of long topographic Rossby type of waves that will be discussed in the next section.

The sheared mean flow may have originated by geostrophic adjustment in response to radial density gradients implied by the observed density change in Fig. 3, resulting from the mixing. However, in rotating fluids, a mean flow may also be generated over continental slopes by tidal rectification: advection of tidal perturbations by the barotropic tide (Huthnance, 1973), or by impinging internal waves (Thorpe, 1999; Maas, 2001). The momentum carried by these internal waves can be partly released, in a process likened to radiation stress divergence of surface waves (Dunkerton et al., 1998). In a non-rotating frame these authors argue that the generated mean flow is in the same direction as the along-isobath component of the obliquely incident internal wave field. The frame's background rotation will break this symmetry and will lead to a preferential orientation of the mean flow (this symmetry breaking is not explicitly discussed, but can be inferred from Thorpe (2000), Fig. 3b).

5.2. Rossby waves

For tidal flow over topography, the tidally rectified baroclinic flow is accompanied by circulation cells in the vertical. The strongest of these predicts down-welling higher up on the slope and upwelling over its foot (Maas and Zimmerman, 1989a,b). This secondary circulation cell may therefore explain the observed increase of density over the foot of the slope (Fig. 3). For the present experimental set-up, where the inner wall is sloping, this mechanism produces an along-isobath, bottom-intensified retrograde flow. The establishment of such a sheared mean flow leads to a venue to another mechanism by means of which the fluid can be mixed. This shear flow may, after all, turn baroclinically or barotropically unstable, leading to the establishment of long, slowly propagating topographic Rossby waves, indications of which have been found in the probe data (not shown).

In the bottom panels of Fig. 7 we show the radial velocity field at a depth of 8 cm, averaged over one forcing period (22.53 s). The two figures are three periods apart. The azimuthal wavelength of the pattern is about 2.0 m and the wave propagates with an azimuthal phase speed of about 3×10^{-3} m s^{-1} (as can be derived from the bottom panels of Fig. 7, using that the wave patterns were three periods apart) in retrograde direction, the direction into which topographic Rossby waves propagate ("westward", towards smaller values of y).

Again considering the top panel of Fig. 7, one observes that the second derivative of the mean flow changes sign at about $r = 525$ cm, or about 25 cm from the sloping wall (at a distance of 8 cm from the fluid surface). At this location a strong shearing flow is present. As discussed in Section 5.1, it is this shearing flow which could cause the instabilities that give rise to the Rossby waves we observe. Furthermore, the shearing mean flow might also act as a barrier that traps the Rossby wave (see e.g. Harlander et al., 2000). This is not inconsistent with the wave shown in Fig. 7, where we see the wave decaying exponentially beyond approximately $r = 525$ cm.

The pattern weakens with depth, thus it is not a bottom trapped mode. The Rossby internal radius of deformation $L_D = N_s H/f$, ($N_s = 2f$, $H = 0.6$ m) is approximately half the wavelength of the wave shown in the bottom panels of Fig. 7 which might explain its quasi-barotropic structure (Pedlosky, 1992, p. 411) and its similarity to topographic Rossby waves.

6. Discussion and conclusions

In this paper we collected experimental evidence for strong mixing in a stratified rotating basin. Internal wave reflection and the formation of a wave attractor were found to be the cause of this mixing of the density profile. As a forcing mechanism for the internal waves we identified a boundary layer eruption at a corner of the domain. We will briefly review each of the mentioned steps.

The remarkably strong mixing of the density profile was discussed in Section 4.1. Since the fluid was not directly disturbed, no obvious source of turbulence is present, and since the basin is axisymmetric, none of the usual mechanisms for mixing are present. This compels us to examine other avenues, and the remainder of the paper was devoted to the detection of internal waves and wave beams that act as a mixing device.

We firstly discussed the boundary layer, and the possibility of its eruption into the interior. Theoretically the boundary layer eruption was made plausible in the appendix, by modification of the theory by MacCready and Rhines (1991), opening the possibility for singularities in boundary layer depth at critical slopes. Experimentally, the internal wave beam that appears to have originated in the boundary layer singularity was very clearly observed (Section 4.2). It is as yet unclear why only waves were generated at the bottom of the shelf. Of course, it is the only location at the boundary where the critical angle is truly existent. However, it was argued that the critical angle is supposed to be 'buried' in sharp corner points. Perhaps this view does not hold, further experimentation could shed some light on this issue.

Using harmonic analysis techniques we obtained phase and amplitude pictures of the vorticity field in radial cross-sections. Wave beams were clearly observed. Furthermore, phase and amplitude strongly suggest the formation of a wave attractor. In Section 4.3 the formation of the wave attractor was presented. Also, in Section 5 we show data consistent with the subsequent generation of a mean flow. Furthermore, we report in this section on Rossby waves, which may also be indicative of strong mixing (Solomon et al., 1993). Considering the above, we believe that we have established the scenario sketched at the end of the introduction. Possibly this insight may be of use to explain mixing in oceans, where the combination of rotation, stratification and boundary topography can similarly lead to efficient localized mixing. This in turn would have consequences in climate research and would impact large scale ocean flow (Wunsch and Ferrari, 2004) and biology (Witbaard et al., 2005).

While the ocean's shape and dimensions are obviously quite distinct from the annulus considered here, both fluid domains possess sloping sides, which renders the presence of wave attractors generic. Whether and where these actually stand out in the face of viscous decay depends on the internal wave's source strength, its frequency, and on ocean shape, stratification and mean currents, all of which determine the internal wave propagation paths. Needless to say that in the face of all these complexities, discovering internal wave attractors and associated mixing in seas and oceans therefore remains a challenge.

Acknowledgments

Help with data acquisition and processing by F. Eijgenraam, and the Coriolis team (S. Vibaud, H. Didelle, O. Praud, A. Fincham, S. Mercier, E. Thivolle and J. Sommeria) is gratefully acknowledged. The access to the experimental facility of the Coriolis Laboratory was supported by the European Commission, Enhancing Access to Research Infrastructures action of the Improving Human Potential programme of FP5, under contract HPRI-CT-1999- 00006. A. N. Swart was funded by NWO as part of the project Numerical Determination of Wave Attractors.

Appendix A. Boundary layer calculations

In this section we consider the boundary layer behaviour of a viscous rotating stratified fluid, at a sloping boundary. We show the existence of a boundary layer 'eruption', a singularity in the equation describing the boundary layer thickness. This eruption would lead to periodic ejection and suction of fluid from the boundary layer which consequently acts as a generator for internal wave beams (see also, Hollerbach and Kerswell, 1995). This concept may be of relevance in the field of oceanography, where the possibility of internal wave generation from boundary layer eruptions has not yet been explored, although indications of them are found in numerical model results on internal wave generation (Drijfhout and Maas, 2008). The merit of the proposed approach lies in the wide range of features that are handled (rotation, stratification, diffusivity, oscillating flows, sloping boundaries). Also we avoid any simplification in the form of balancing certain terms explicitly in the equations. The drawback is the assumption of an axisymmetric domain of large radius, and the neglect of velocity variations parallel to the boundary. However, the latter assumption is standard and we believe our method has great generality at the price of few assumptions.

We start with the general set of equations governing perturbations in rotating stratified fluids. We assume gravity $\mathbf{g} = -g\hat{\mathbf{z}}$ to be antiparallel with the frame rotation vector $\boldsymbol{\Omega} = \Omega_0\hat{\mathbf{z}}$ where $\hat{\mathbf{z}}$ represents a vertical unit vector. More detailed explanation may be found in e.g. Pedlosky (1992) or LeBlond and Mysak (1978). As is common under the Boussinesq approximation, we set density $\rho = \rho_* + \rho_0(z) + \rho'(\mathbf{x}, t)$. The linearized equations of motion in a cylindrical $(\hat{\mathbf{r}}, \hat{\theta}, \hat{\mathbf{z}})$-frame for the velocities $\mathbf{u} = (u, v, w)$, buoyancy $b = -g\rho'/\rho_*$ and reduced pressure P may be written

$$\begin{aligned} &\mathbf{u}_t + \mathbf{f} \times \mathbf{u} = -\nabla P + b\hat{\mathbf{z}} + \nu\vec{\Delta}\mathbf{u}, \\ &b_t + N^2\mathbf{u}\cdot\hat{\mathbf{z}} = \kappa\Delta b, \\ &\nabla\cdot\mathbf{u} = 0. \end{aligned} \tag{5}$$

Here $f = 2\Omega_0$ is twice the angular velocity, N is the stability frequency, defined by $N^2 = -g\rho_*^{-1}d\rho_0/dz$, and ν and κ represent the dynamic viscosity and diffusivity respectively. Next, we use axisymmetry and set all derivatives with respect to the θ coordinate to zero.[1] The scalar Laplacian in cylindrical coordinates then becomes

$$\Delta = \frac{\partial^2}{\partial r^2} + \frac{1}{r}\frac{\partial}{\partial r} + \frac{\partial^2}{\partial z^2},$$

and the vector Laplacian is given by

$$\vec{\Delta} = \left(\Delta - \frac{1}{r^2}, \Delta - \frac{1}{r^2}, \Delta\right).$$

In our experiment, the radius of the axisymmetric basin is large compared to depth H, thus $r \gg H$. This justifies setting all terms involving r^{-2} to zero. Next, define the following differential operators,

$$\begin{aligned} \mathcal{L} &= \partial_t - \nu\Delta, \\ \mathcal{T} &= \partial_t - \kappa\Delta. \end{aligned}$$

In terms of these operators the governing set of equations reads

$$\mathcal{L}u - fv = -P_r, \tag{6}$$

$$\mathcal{L}v + fu = 0, \tag{7}$$

$$\mathcal{L}w = -P_z + b, \tag{8}$$

$$\mathcal{T}b + N^2 w = 0, \tag{9}$$

$$\nabla\cdot\mathbf{u} = 0. \tag{10}$$

We now continue with the reduction of the above set of equations into one equation (for the stream function). Firstly, cross differentiating the first and third equation and subtracting them yields,

$$\mathcal{L}(u_z - w_r) - fv_z + b_r = 0.$$

The velocity component v may be eliminated by applying $\mathcal{L}$ to the above equation and substituting (7),

$$\mathcal{L}^2(u_z - w_r) + f^2 u_z + \mathcal{L}b_r = 0.$$

Finally, the buoyancy is eliminated by differentiating (9) with respect to r, applying $\mathcal{T}$ to the above equation, and substituting,

$$\mathcal{T}\mathcal{L}^2(u_z - w_r) + f^2\mathcal{T}u_z - \mathcal{L}N^2(z)w_r = 0.$$

[1] Instead of setting derivatives to zero, there are other possibilities. E.g., separation in the form $\mathbf{u}(r, \theta, z) = \mathbf{f}(r, z)\mathbf{g}(\theta)$, with a 2π-periodic function g, but this would complicate the discussion.

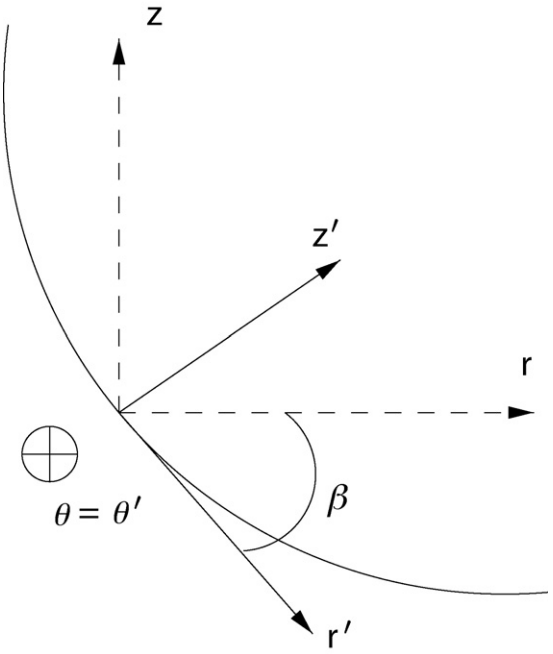

Fig. 8. The local coordinate system (primed) for use in the boundary layer calculations. The curve represents the boundary of the domain. The inward normal is z', while r' is tangent to the boundary.

We still need to satisfy the continuity equation $\nabla \cdot \mathbf{u} = r^{-1}\partial_r(ru) + w_z = 0$, which may be accomplished by introducing the stream function Ψ, satisfying $(\Psi_z, -\Psi_r) = (ru, rw)$. This casts the equations in the form

$$\mathcal{T}(\mathcal{L}^2 + f^2)r^{-1}\Psi_{zz} + \mathcal{L}(\mathcal{T}\mathcal{L} + N^2(z))\partial_r(r^{-1}\Psi_r) = 0. \tag{11}$$

At the boundary of the fluid domain the oscillating fluid has to adjust to the boundary. We are interested in the boundary layer behaviour and consider a small segment of the boundary locally. We describe this segment *locally* as plane, inclined at an angle β with the horizontal and parallel to the θ axis. We rotate the coordinate frame in order to have the z' axis perpendicular to the slope, the θ axis cross-slope and the r' axis along-slope. We add a prime to quantities in the rotated system. See Fig. 8 for a schematic picture of the local coordinate system. We need the following transformations

$$\begin{pmatrix} e'_1 \\ e'_2 \\ e'_3 \end{pmatrix} = \begin{pmatrix} \cos(\beta) & 0 & -\sin(\beta) \\ 0 & 1 & 0 \\ \sin(\beta) & 0 & \cos(\beta) \end{pmatrix} \begin{pmatrix} e_1 \\ e_2 \\ e_3 \end{pmatrix}.$$

The relevant differential operators transform as

$$\partial_{rr} = \cos^2(\beta)\partial_{r'r'} + \sin^2(\beta)\partial_{z'z'} - 2\sin(\beta)\cos(\beta)\partial_{r'z'},$$
$$\partial_{zz} = \sin^2(\beta)\partial_{r'r'} + \cos^2(\beta)\partial_{z'z'} + 2\sin(\beta)\cos(\beta)\partial_{r'z'},$$
$$\partial_{rr} + \partial_{zz} = \partial_{r'r'} + \partial_{z'z'}.$$

At this point we need an additional simplification and we assume that in the boundary layer, derivatives with respect to r' are negligible compared to derivatives with respect to z'. This means that we assume rapid variation in the boundary layer z' direction (needed to adjust the interior of the

fluid to the boundary) and slow variation along the boundary layer. This gives us

$$\partial_{rr} = \sin^2(\beta)\partial_{z'z'},$$
$$\partial_{zz} = \cos^2(\beta)\partial_{z'z'},$$
$$\Delta = \partial_{z'z'}.$$

The Eq. (11) for the boundary layer becomes

$$[\mathcal{T}(\mathcal{L}^2 + f^2)\cos^2(\beta) + \mathcal{L}(\mathcal{T}\mathcal{L} + N^2(z))\sin^2(\beta)]\Psi_{z'z'} = 0.$$

This general equation is much too formidable to solve directly and we simplify by assuming monochromatic wave motion, i.e. we look for solutions of the form

$$\Psi(r', z', t) = \Re[\tilde{\Psi}(r', z')e^{i\omega t}]. \tag{12}$$

We continue by rewriting the equation in terms of the along-slope velocity $u = \tilde{\Psi}_{z'}/r'$,

$$i\omega[\tilde{f}^2 + \tilde{N}^2 - \omega^2]u^{(1)} + [\omega^2(2\nu + \kappa) - (\kappa\tilde{f}^2 + \nu\tilde{N}^2)]u^{(3)} + \nu\omega[\nu + 2\kappa]u^{(5)} - \kappa\nu^2 u^{(7)} = 0, \tag{13}$$

where $u^{(n)} = d^n u'/dz'^n$, and $\tilde{f} = \cos(\beta)f$ and $\tilde{N} = \sin(\beta)N$. As follows from (7), the azimuthal velocity component, v, satisfies the same equation.

There are two cases of special interest to our setting, oscillating and non-oscillating flow. We start our exposition with the latter.

When we have a steady flow, $\omega = 0$ and (13), cast in terms of v, reduces to

$$\frac{\sigma\tilde{N}^2 + \tilde{f}^2}{\nu^2} v^{(3)} = -v^{(7)},$$

with $\sigma = \nu/\kappa$, the Prandtl number. The velocity is now a real valued function. The solution to this ordinary differential equation is given by (dropping the primes on z):

$$v(z) = e^{z/h}[b_1 e^{iz/h} + b_2 e^{-iz/h}] + e^{-z/h}[b_3 e^{iz/h} + b_4 e^{-iz/h}] + b_5 + b_6 z + b_7 z^2,$$

with

$$h = \left(\frac{4\nu^2}{\sigma\tilde{N}^2 + \tilde{f}^2}\right)^{1/4} \tag{14}$$

and constants $b_1, \ldots, b_7$. We consider the following boundary conditions,

$$v(0) = -V,$$
$$\lim_{z\to\infty} v(z) = 0.$$

The given constant V represents the amplitude of the azimuthal interior 'tidal' flow far above the bottom, which at the bottom needs to be cancelled by the boundary layer velocity. Far away from the boundary, however, the boundary layer velocity should vanish, which amounts to the second condition stated above. In order to satisfy the boundary condition at infinity we require $b_1 = b_2 = b_5 = b_6 = b_7 = 0$ and we find that the real part of the velocity is given by

$$v(z) = e^{-z/h}[c_1 \cos(z/h) + c_2 \sin(z/h)],$$

with constants $c_{1,2}$ related to $b_{3,4}$. The boundary condition at $z = 0$ then implies

$$v(z) = e^{-z/h}[-V \cos(z/h) + c_2 \sin(z/h)]$$

for some unknown constant c_2. Note that this coefficient may in principle be determined by considering the vanishing of the radial velocity component u at the boundary. Since viscosity (ν) and diffusivity (κ) are assumed to be small in (13), we are in the case $h \to 0$. When h tends to zero, the exponential function is relevant on spatial scales $z = \mathcal{O}(h)$. We conclude that the boundary layer height extends over a distance h above the bottom.

We now continue with the treatment of oscillatory flows. In (13), again phrased in terms of the azimuthal velocity, we also neglect products of κ and ν since these are small parameters and obtain the following differential equation

$$\frac{i\omega}{\kappa}\frac{\tilde{f}^2+\tilde{N}^2-\omega^2}{\sigma(\tilde{N}^2-2\omega^2)+(\tilde{f}^2-\omega^2)}v^{(1)}=v^{(3)}$$

with $\sigma=\nu/\kappa$.

Recall that the oscillatory nature of the flow was introduced by $v(z,t)=\Re(e^{i\omega t}v(z))$. By definition of differentiation of complex valued functions $f_x(x)=\partial_x\Re(f)+i\partial_x\Im(f)$ we obtain a system of equations, from which we obtain the equation for the real part of v, denoted by v_r,

$$-\frac{\omega^2}{\kappa^2}\left(\frac{\tilde{N}^2/(\tilde{N}^2-2\omega^2)-\tilde{\lambda}^2}{\sigma-\tilde{\lambda}^2}\right)^2 v_r^{(1)}=v_r^{(5)},$$

with $\tilde{\lambda}^2=(\omega^2-\tilde{f}^2)/(\tilde{N}^2-2\omega^2)$. We proceed as in the non-oscillating case to find the physically acceptable boundary layer depth given by

$$h_1=\sqrt{\frac{2\kappa}{\omega}\left(\frac{\sigma-\tilde{\lambda}^2}{\tilde{N}^2/(\tilde{N}^2-2\omega^2)-\tilde{\lambda}^2}\right)}. \tag{15}$$

In the case of sloping walls our results differ from previous results. For example, for steady flows ($\omega=0$), Garrett et al. (1993) found that the boundary layer over a sloping bottom is thinner as compared to a flat bottom, by a factor $(1+\sigma N^2\sin^2(\beta)/f^2)^{-1/4}$, while we find from (14) a factor $(1+\sigma(N^2-f^2)\sin^2(\beta)/f^2)^{-1/4}$.

The difference is insignificant for $N\gg f$, but for oscillating flow the results differ more. We can rewrite (15) as

$$h_1(\beta)=\sqrt{\frac{2\kappa}{\omega}\left(\frac{f^2+\sigma\tilde{N}^2-[\omega^2(1+2\sigma)+f^2\,\sin^2(\beta)]}{f^2+\tilde{N}^2-[\omega^2+f^2\,\sin^2(\beta)]}\right)}.$$

The terms in square brackets are not present in Garrett et al. (1993). The main difference with the results from those authors is that they assume $w=0$ from the onset and neglect the term $\partial P/\partial x$. The term $\nu\Delta w$ was replaced by a Reynolds stress component $-\partial(\bar{w}^2)/\partial z$.

An important observation is that because of the presence of our additional terms, the depth may become singular for

$$\omega^2=\tilde{N}^2+\tilde{f}^2=N^2\,\sin^2(\beta)+f^2\,\cos^2(\beta).$$

Comparing this with the dispersion relation (3) we find boundary layer singularities for

$$\beta=k\pi\pm\alpha,\quad k\in\mathbb{N}. \tag{16}$$

Thus, for fixed frequency ω, stability frequency N and Coriolis parameter f, the boundary layer may erupt at certain specific local angles (β) of the boundary. This is the so-called critical angle, where the bottom slope is identical to that of the characteristics. This connects the boundary layer directly to the interior of the fluid, opening the possibility for forcing of waves. See also the laboratory experiments described in Gostiaux and Dauxois (2007) where wave beams were clearly seen to emanate from critical slopes albeit in their case of convex slope these beams are tangent to the slope.

Furthermore, we note that our results generalize classical results. For example, for $N=0$, for steady flows we find from (14) a boundary layer scale of $h=[2\nu/(f\,\cos(\beta))]^{1/2}$ (see also MacCready and Rhines (1991), Eq. (2.9)), which simplifies to the well known Ekman layer depth of $[2\nu/f]^{1/2}$ at a flat bottom.

References

Baines, P.G., 1982. On internal tide generation methods. Deep-Sea Res. 29 (3A), 307–338.
Batchelor, G.K., 1967. An Introduction to Fluid Dynamics. Cambridge University Press, Cambridge.

Beardsley, R.C., 1970. An experimental study of inertial waves in a closed cone. Stud. Appl. Math. 49, 187–196.
Drijfhout, S., Maas, L.R.M., 2008. Impact of channel geometry and rotation on the trapping of internal tides. J. Phys. Oceanogr. 37, 2740–2763.
Dunkerton, T.J., Delisi, D.P., Lelong, M.-P., 1998. Alongslope current generation by obliquely incident internal gravity waves. Geophys. Res. Lett. 25, 3871–3874.
Fincham, A.M., Spedding, G.R., 1997. Low-cost, high resolution dpiv for measurement in turbulent flows. Exp. Fluids 23, 449–462.
Garrett, C., MacCready, P., Rhines, P., 1993. Boundary mixing and arrested Ekman layers: rotating stratified flow near a sloping boundary. Annu. Rev. Fluid Mech. 25, 291–323.
Gostiaux, L., Dauxois, T., 2007. Laboratory experiments on the generation of internal tidal beams over steep slopes. Phys. Fluids, 19.
Greenspan, H.P., 1968. The Theory of Rotating Fluids. Cambridge University Press.
Harlander, U., Maas, L.R.M., 2007. Two alternatives for solving hyperbolic boundary value problems of geophysical fluid dynamics. J. Fluid Mech. 588, 331–351.
Harlander, U., Schönfeld, H.J., Metz, W., 2000. Rossby waveguides in high-latitude shear flows with boundaries. J. Geophys. Res. 105 (C7), 17,063–17,078.
Hazewinkel, J.P., van Breevoort, S.B., Dalziel, L.R., Maas, M., 2008. Observations on the wave number spectrum and evolution of an internal wave attractor in a two-dimensional domain. J. Fluid Mech. 598, 373–382.
Hollerbach, R., Kerswell, R.R., 1995. Oscillatory internal shear layers in rotating and precessing flows. J. Fluid Mech. 298, 327–339.
Huthnance, J.M., 1973. Tidal current asymmetries over the Norfolk Sandbanks. Estuarine Coastal Mar. Sci. 1, 89–99.
Kerswell, R.R., 1995. On the internal shear layers spawned by the critical regions in oscillatory Ekman boundary layers. J. Fluid Mech. 298, 311–325.
Lam, F.-P.A., Maas, L.R.M., 2008. Internal wave focusing revisited; a reanalysis and new theoretical links. Fluid Dyn. Res. 40, 95–122.
LeBlond, P.H., Mysak, L.A., 1978. Waves in the Ocean. Elsevier.
Ledwell, J.R., Montgomery, E.T., Polzin, K.L., Laurent, St.L.C., Schmidt, R.W., Toole, J.M., 2000. Evidence for enhanced mixing over rough topography in the abyssal ocean. Nature 403 (13).
Legg, S., Adcroft, A., 2003. Internal wave breaking at concave and convex continental slopes. J. Phys. Oceanogr., 33.
Lyashenko, A.A., Smiley, M.W., 1995. The Dirichlet problem for the semilinear vibrating string equation in a class of domains with corner points. J. Math. Anal. Appl. 189, 872–896.
Maas, L.R.M., Benielli, D., Sommeria, J., Lam, F.-P.A., 1997. Observation of an internal wave attractor in a confined stably stratified fluid. Nature 388, 557–561.
Maas, L.R.M., van, J.J.M., Haren, 1987. Observations on the vertical structure of tidal and inertial currents in the central North Sea. J. Mar. Res. 45, 293–318.
Maas, L.R.M., Lam, F.-P.A., 1995. Geometric focusing of internal waves. J. Fluid Mech. 300, 1–41.
Maas, L.R.M., Zimmerman, J.T.F., 1989a. Tide-topography interactions in a stratified shelf sea. ii. Bottom trapped internal tides and baroclinic residual currents. Geophys. Astrophys. Fluid Dyn. 45, 37–69.
Maas, L.R.M., Zimmerman, J.T.F., 1989b. Tide-topography interactions in a stratified shelf sea. i. Basic equations for quasi-nonlinear internal tides. Geophys. Astrophys. Fluid Dyn. 45, 1–35.
Maas, L.R.M., 2001. Wave focusing and ensuing mean flow due to symmetry breaking in rotating fluids. J. Fluid Mech. 437, 13–28.
Maas, L.R.M., 2005. Wave attractors: linear yet nonlinear. Int. J. Bifurcation Chaos 15, 2757–2782.
MacCready, P., Rhines, P.B., 1991. Buoyant inhibition of Ekman transport on a slope and its effect on stratified spin-up. J. Fluid Mech. 223, 631–661.
Manders, A.M.M., Maas, L.R.M., 2003. Observations of inertial waves in a rectangular basin with one sloping boundary. J. Fluid Mech. 493, 59–88.
Manders, A.M.M., Maas, L.R.M., 2004. On the three-dimensional structure of the inertial wave field in a rectangular basin with one sloping boundary. Fluid Dyn. Res. 35, 1–21.
Pedlosky, J., 1992. Geophysical Fluid Dynamics. Springer Verlag.
Prandle, D., 1982. The vertical structure of tidal currents and other oscillatory flows. Continen. Shelf Res. 1 (2), 191–207.
Ramsden, D., 1995. Response of an oceanic bottom boundary layer on a slope to interior flow. Part ii. Time-dependent interior flow. J. Phys. Oceanogr. 25, 1688–1695.
Solomon, T.H., Holloway, W.J., Swinney, H.L., 1993. Shear flow instabilities and Rossby waves in barotropic flow in a rotating annulus. Phys. Fluids 5 (8).
Sommeria, J., 2007. Personal communication.
Staquet, C., Sommeria, J., 2002. Internal gravity waves: from instabilities to turbulence. Annu. Rev. Fluid. Mech. 34, 559–593.
Storch, H.V., Zwiers, F.W., 1999. Statistical Analysis in Climate Research. Cambridge.
Swart, A.N., Sleijpen, G.L.G., Maas, L.R.M., Brandts, J., 2007. Numerical solution of the two dimensional Poincaré equation. J. Appl. Comput. Math. 200 (1), 317–341.
Swart, A.N., 2007. Internal Waves and the Poincaré Equation. Numerical Computation and Laboratory Experiments. PhD thesis. University of Utrecht, 2007.
Thorade, H., 1928. Gezeitenuntersuchungen in der Deutschen Bucht der Nordsee. Deutsche Seewarte 46 (3).
Thorpe, S.A., 1999. The generation of alongslope currents by breaking internal waves. J. Phys. Oceanogr. 29, 29–38.
Thorpe, S.A., 2000. The effects of rotation on the nonlinear reflection of internal waves from a slope. J. Phys. Oceanogr. 30, 1901–1909.
Witbaard, R., Daan, R., Mulder, M., Lavaleye, M., 2005. The mollusc fauna along a depth transect in the faroe shetland channel: Is there a relationship with internal waves? Mar. Biol. Res. 1 3, 186–201.
Wunsch, C., Ferrari, R., 2004. Vertical mixing, energy and the general circulation of the oceans. Annu. Rev. Fluid Mech. 36, 281–314.